Conference Proceedings

The NanoMed and Sensors 2024 International Joint Conference

Barcelona, Spain - Oct 23 to 25, 2024

DOI:
https://doi.org/10.26799/cp-sms-nanomed-sensors-egf-2024

Proceedings of the NanoMed 2024 International Conference
Barcelona, Spain, 23 – 25 October 2024
DOI: https://doi.org/10.26799/cp-sms-nanomed-sensors-egf-2024

PIC micelles encapsulating medical Cu-64 as a Drug Delivery System for Cancer Therapy

Mary Alfonse George Mikhail[1], Nobuya Hayashi[1,2], Taisei Eto[1], Kazuaki Tsukada[3], Akihiro Kishimura[4,5], and Hiroshi Kamizawa[6]

[1]Kyushu University, Interdisciplinary Graduate School of Engineering Sciences, Fukuoka, Japan
[2]Kyushu University, International Research Centre for Space and Planetary Environmental Science, Fukuoka, Japan
[3]Japan Atomic Energy Agency, Ibaraki, Japan
[4]Kyushu University, Department of Applied Chemistry, Faculty of Engineering, Fukuoka, Japan
[5]Kyushu University, Centre for Molecular Systems, Fukuoka, Japan
[6]Kyushu University, Graduate School of Systems Life Sciences, Fukuoka, Japan

Abstract

Copper-64 (^{64}Cu) is a promising theranostic radionuclide utilized for positron emission tomography (PET) in cancer diagnosis and as a potential therapeutic candidate. This radionuclide emits widely used therapeutic particles β^- and Auger electrons, known to have lethal effects on cancer cells. Selecting an appropriate Drug Delivery System (DDS) is crucial to studying the impact of ^{64}Cu on cancer cells. Polyion complexes (PICs) are up-and-coming DDS designed to effectively deliver genes, small nucleic acids, proteins, and charged macromolecular drugs. PIC formation can occur in aqueous media without organic solvent, and the preparation process is remarkably straightforward. Therefore, it is a simple and versatile technique to encapsulate $CuCl_2$ ions to target cancer cells. In this study, $^{64}CuCl_2$, free and chelated with DOTA, was successfully encapsulated within the PIC micelles. TLC results indicated that the chelated $^{64}CuCl_2$ had a higher affinity for PIC micelles. Furthermore, *in vitro* experiments were conducted to evaluate the impact of the encapsulated copper on both a normal cell line (HaCaT) and a cancerous cell line (HSC-3). The results showed that the proliferation of normal cells remained unaffected by adding PIC micelles, $CuCl_2$, or encapsulated $CuCl_2$ micelles, indicating no toxicity. Conversely, cancer cells showed higher mortality rates when exposed to free $CuCl_2$ or encapsulated $CuCl_2$ micelles, confirming the effective delivery of Cu^{2+} to these cells. Additionally, significantly elevated mortality rates were observed in the cancer cell line when treated with DOTA.

Keywords: Copper-64, Poly Ion Complex (PIC) micelles, Drug Delivery System (DDS), Cancer, Theranostics.

1. Introduction

Copper is an essential trace element integral to various enzymes, including ferroxidases, cytochrome c oxidase, superoxide dismutase, tyrosinase, lysyl oxidase, and dopamine beta-hydroxylase. Copper is found in all organs and is most concentrated in the liver and brain. Its absorption and regulation are managed by liver-controlled homeostatic mechanisms, with most copper excreted via bile through the ATP7B copper transporter. In contrast, only a small fraction is excreted in the urine.[1] Maintaining precise control over copper homeostasis -covering uptake, transport, storage, and excretion- is critical for health. Disruptions in this balance are implicated in genetic disorders like Wilson's disease and Menkes disease, as well as in cancer. In cancer, copper contributes to disease progression by facilitating cell proliferation, angiogenesis, and metastasis.[2] These findings emphasize copper's essential role in cancer biology and its potential as a target for therapeutic strategies. Two promising approaches for leveraging copper in cancer therapy have emerged. First, the copper chelation which reduces copper availability within tumor cells, thereby inhibiting copper-dependent processes such as angiogenesis and cell proliferation, ultimately slowing tumor growth and promoting cancer cell death. The second approach involves using copper ionophores to increase intracellular copper levels. By delivering copper ions directly into cells, this method exploits the tendency of cancer cells to retain excess copper. Elevated copper levels induce reactive oxygen species (ROS) production, leading to toxic damage and cell death, as cancer cells are particularly vulnerable to oxidative stress.[3]

Nearly all tumors experience continuous or intermittent hypoxic phases, which can drive cellular transformation and encourage tumor microenvironment (TME) cells to function as pro-tumoral agents. Considering these hypoxic conditions, radiopharmaceuticals have focused on developing various markers that can be effectively localized or modified within tumor sites. Radiopharmaceuticals play a critical role in diagnostic and non-

DOI: https://doi.org/10.26799/cp-sms-nanomed-sensors-egf-2024

invasive therapeutic procedures, especially for cancer diagnosis and treatment, which is the primary application of medical radionuclides. Copper-64 (^{64}Cu) is an appealing radionuclide for theranostic applications due to its unique decay characteristics, enabling diagnostic imaging and therapeutic interventions. It decays through three modes: 1) beta emission (β–) at 38.48%, 2) positron emission (β+) at 17.49%, and 3) electron capture (EC) at 43.56% (**Fig.1**). The positron emission enables positron emission tomography (PET), a widely used technique in cancer diagnostics. With a half-life of 12.7 hours, ^{64}Cu allows for extended imaging and monitoring, making it feasible to track biological processes up to two days post-administration. Furthermore, its beta particle emissions make it well-suited for therapeutic applications, as these particles, along with Auger electrons, have demonstrated cytotoxic effects on cancer cells, enhancing its potential as a dual-purpose theranostic agent.[4]

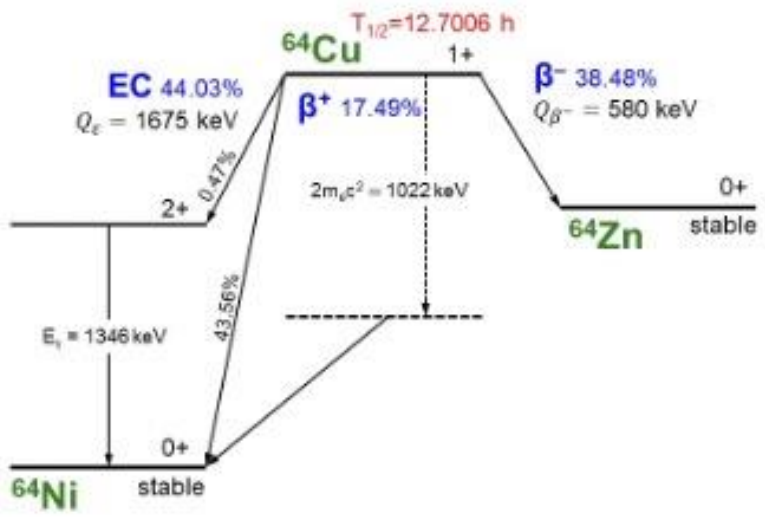

Fig.1:The Decay scheme of ^{64}Cu is shown with the transition probability of a single decay.

Selecting an appropriate Drug Delivery System (DDS) is essential for investigating the effects of copper isotopes in non-radioactive and radioactive forms on cancer cells. Polyion Complexes (PICs) represent a promising DDS designed to facilitate the effective delivery of genes, small nucleic acids, proteins, and charged macromolecular drugs. One of the significant advantages of PICs is their ability to form in aqueous media without the need for organic solvents, making the preparation process notably straightforward. Typically, PICs are created by simply mixing oppositely charged copolymers of polyethylene glycol (PEG) and charged polypeptides (**Fig.2**).[5] Notably, charge pairs of PICs can be crosslinked to enhance their robustness via amido-bond formation, which is helpful for copper ion encapsulation. In this study, we examined the encapsulation efficiency of copper within crosslinked PIC micelles. Subsequently, *in vitro* experiments were performed to assess copper's effects on cancer cells, employing the two previously discussed strategies for copper-based cancer treatment.

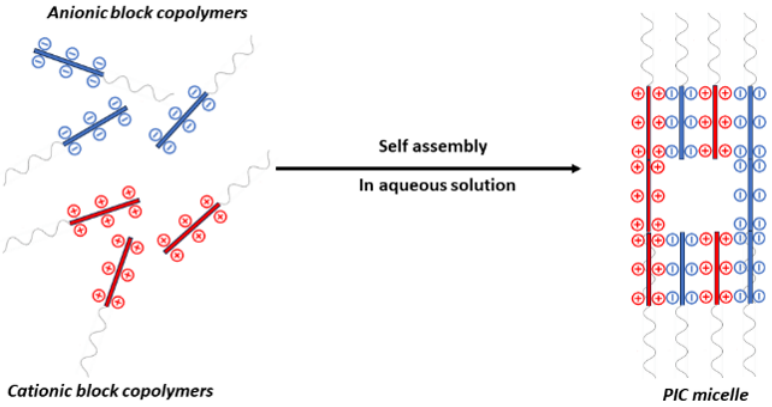

Fig. 2: PIC micelle formation

DOI: https://doi.org/10.26799/cp-sms-nanomed-sensors-egf-2024

2. Experiment

2.1. Assessment of Copper Encapsulation

Crosslinking of the PIC micelles is crucial for micelle stabilization. 1-Ethyl-3-(3-dimethylaminopropyl) carbodiimide (EDC) is used as a crosslinker, and Cu^{2+} ions are loaded before application (**Fig. 3**). Cu encapsulation was evaluated using Scanning Electron Microscopy (SEM) and in case of ^{64}Cu, the encapsulation was assessed using Thin-Layer Chromatography (TLC). In the latter case, we evaluated the encapsulation of free ^{64}Cu and ^{64}Cu-DOTA complex.

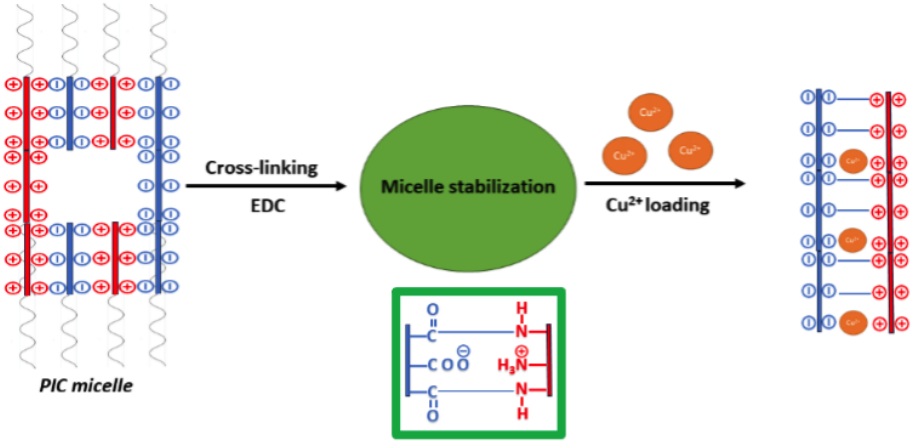

Fig. 3: Stabilization of PIC Micelles with Subsequent Cu^{2+} Loading

2.2. In-vitro experiments

To investigate the toxicity of PIC micelles and Cu^{2+} ions, *in vitro* experiments were conducted using both normal and cancer cell lines. HaCat cells (human epidermal keratinocytes) were selected for the normal cell line, while the HSC-3 cell line (human oral squamous carcinoma cells with high metastatic potential) represented cancer cells. Both cell lines were sourced from the Japanese Cancer Research Resources Bank (JCRB) Cell Bank. Cells were cultured in MEM-α medium supplemented with 10% fetal bovine serum (FBS) and 1% penicillin. Cultivation periods differed: HaCat cells were incubated for 48 hours, while HSC-3 cells were cultured for 72 hours. Once proliferation was achieved, cells were seeded into 96-well plates and incubated for 24 hours. Following this incubation, the encapsulated Cu^{2+} ions were added alongside two control groups: one containing PIC micelles and the other containing Cu^{2+} alone. The cells were then incubated for an additional 24 hours. Finally, cell viability was measured using a microplate reader set to a wavelength of 450 nm.

3. Results and Discussion

3.1. Assessment of Copper Encapsulation

The SEM elemental mapping confirmed the presence of Cu within the PIC micelles, as shown in **Fig. 4**. TLC analysis also demonstrated that chelated $^{64}CuCl_2$ exhibited a strong affinity for PIC micelles, suggesting efficient encapsulation. This high encapsulation efficiency may be attributed to the large number of carboxylate groups at the side chains and amide bonds found in polypeptide main chains and crosslinking points, which can show a high affinity to Cu ions.

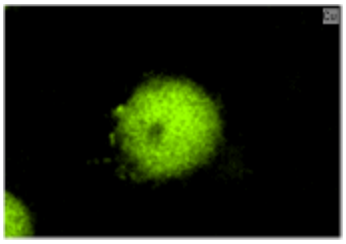

Fig. 4: SEM element mapping showing Cu inside the PIC micelle.

DOI: https://doi.org/10.26799/cp-sms-nanomed-sensors-egf-2024

3.2. *In vitro* experiments

As shown in **Fig. 6**, microplate reader results indicate that PIC micelles exhibit no toxicity toward the HaCat cell line (normal cells). These cells maintained normal proliferation when treated with Cu^{2+} ions, supporting the hypothesis that normal cells can tolerate moderate increases in Cu^{2+} levels and the associated ROS production. In contrast, the HSC-3 cancer cell line exhibited a significant reduction in cell numbers when exposed to Cu^{2+} ions, underscoring the efficacy of the Cu ionophore strategy as a targeted cancer treatment.

Fig. 7 further demonstrates the effect of Cu^{2+} in comparison with DOTA on the HSC-3 cancer cell line. The chelation approach with DOTA substantially reduced cancer cell proliferation, effectively inducing cell death. These findings support both therapeutic strategies for Cu-based cancer treatment.

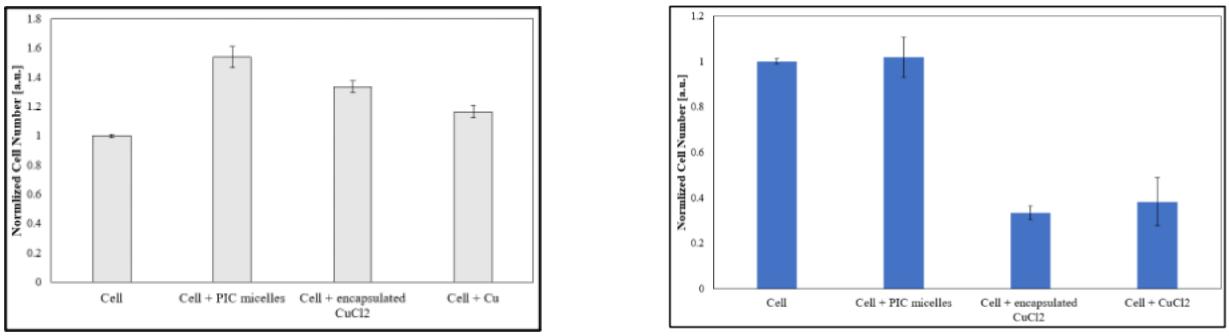

Fig. 5: The left panel illustrates the effects of PIC micelles and Cu^{2+} ions on the normal HaCat cell line, while the right panel displays their impact on the HSC-3 cancer cell line.

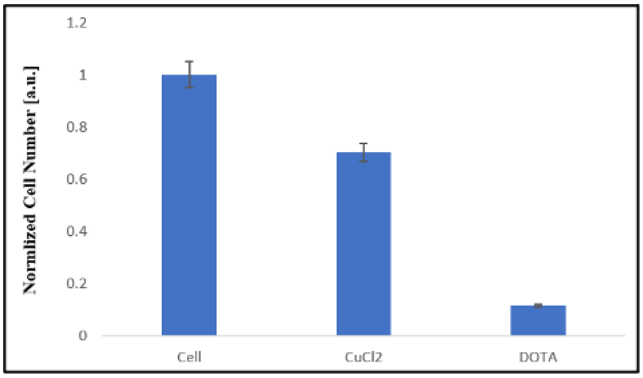

Fig. 6: Demonstration of the effects of Cu^{2+} and DOTA on the HSC-3 cancer cell line.

4. Conclusion

Given the therapeutic and diagnostic potential of copper, both in its non-radioactive and radioactive forms, in cancer treatment, this study explored two key strategies: increasing or decreasing intracellular Cu levels. Our focus was to harness the benefits of Cu by selecting a suitable drug delivery system (DDS) to assess its effects on cancer cells. Cu encapsulation within PIC micelles was successfully achieved, enabling targeted delivery to cancer cells. This targeted approach resulted in higher cancer cell mortality, confirming the effective delivery and therapeutic impact of Cu^{2+} on these cells.

Acknowledgments

We thank the JST Mirai, Grant Number JPMJSP2136, for funding and supporting this work.

References

1. Dag G.Ellingsen, Nina Horn, and Jan Aaseth, *Handbook on the toxicology of metals*, Chapter 26: Copper, Elsevier, 529-546, 2007.
2. Liyun Chen, Junxia Min, and Fudi Wang, *Copper homeostasis and cuproptosis in health and disease,* Signal Transduction and Targeted Therapy, **7**, Article number: 378, 2022.
3. Xiaolong Tang, Zaihua Yan, Yandong Miao, Wuhua Ha, Zheng Li, Lixia Yang and Denghai Mi, *Copper in cancer: from limiting nutrient to therapeutic target,* Frontiers in Oncology, **13**, 2023.

DOI: https://doi.org/10.26799/cp-sms-nanomed-sensors-egf-2024

4. Mary Alfonse George Mikhail, Tadahiro Kin, Taisei Eto, and Kazuaki Tsukada, *Improved extraction efficiency of radioactive copper produced via accelerator neutrons method through phosphate buffer enhanced column pre-treatment*, Scientific Reports, **14**, Article number: 27132, 2024.
5. Akihiro Kishimura, *Development of polyion complex vesicles (PICsomes) from block copolymers for biomedical applications,* Polymer Journal, **45**, 892–897, 2013.

Proceedings of the NanoMed 2024 International Conference
Barcelona, Spain, 23 – 25 October 2024
DOI: https://doi.org/10.26799/cp-sms-nanomed-sensors-egf-2024

Tuning Fibrinogen Adsorption on Layer-by-Layer Built PAA/PAH Multilayer Films: Effect of Deposition Conditions and Hydrophilicity

B. Borisova[1], T. Andreeva[1,2,*], R. Tzoneva[1*], R. Krastev[2]

[1] Institute of Biophysics and Biomedical Engineering, Bulgarian Academy of Sciences, Acad. G. Bonchev Str., Bl. 21, Sofia 1113, Bulgaria, email: tzoneva@bio21.bas.bg, bborissova@bio21.bas.bg
[2] Faculty Life Sciences, Reutlingen University, Alteburgstraße 150, 72762 Reutlingen, Germany, email: Tonya.Andreeva@Reutlingen-University.DE, Rumen.Krastev@Reutlingen-University.DE
[*] Corresponding authors

Abstract

This work investigates the relationship between adsorption of fibrinogen (FNG) on solid surfaces modified by polyelectrolyte multilayer films (PEM) and their surface properties. A pair of weak polyelectrolytes, polyacrylic acid and poly (allylamine hydrochloride), was used to prepare four different PEM films by assembly under different deposition conditions. The thickness of the films was examined by ellipsometry and surface wettability was analyzed by the contact angle method. The Bradford assay and ELISA method were used to quantify FNG adsorption and conformation onto different PEMs. The study contributes to understanding the impact of hydrophilicity and film structure on protein adsorption, and can be used to design biocompatible biomedical devices.

Keywords: protein adsorption, surface modification, polyelectrolyte multilayers, biofunctionalization

1. Introduction

Polyelectrolyte (PE) multilayers (PEM) are now a well-established concept for modifying the properties of solid substrates as biomaterials by creating nano-thick films to improve their biocompatibility [1-2]. PEMs provide precise and controlled modification of surface properties without affecting the micro topology of the materials or their bulk properties. The selection of polyelectrolyte pairs and process parameters during PEM fabrication dictates their physicochemical properties and enables the fine-tuning of protein adsorption onto PEM-coated biomaterials, which is critical in biomedicine field, particularly for the design of blood-contacting devices [3]. Fibrinogen (FNG) adsorption pattern onto biomaterial surfaces is crucial for their blood compatibility [4]. Several studies suggested that platelet adhesion and activation onto biomaterial surfaces, which are prerequisites for thrombus formation, might be affected particularly by the conformation of FNG upon adsorption [5-7]. The adsorption profile of FNG depends strongly on the physicochemical properties of the surface such as surface wettability, surface charge density, and others [8-9]. In this study we used PEM to create biocompatible coatings on biomaterials with diverse well-defined surface properties. The results indicate a correlation between the nature of the outermost polyelectrolyte layer, surface wettability and FNG adsorption. The obtained data can guide the rational design of biocompatible surfaces with controlled protein adsorption.

2. Materials and methods

2.1. PEM build-up

Polyelectrolyte multilayer films were assembled using a layer-by-layer dip coating technique described in more details in [10], applying polyethyleneimine (PEI, Sigma Aldrich, branched, Mw ~750 kDa) as a precursor layer and continuing with polyacrylic acid (PAA, Sigma Aldrich, Mw ~100 kDa) and poly (allylamine hydrochloride) (PAH, Thermo Scientific, Mw120-200 kDa). The deposition was performed from water solutions with PE concentration of 2 mg/ml in presence of 0.5 M NaCl. Four types of PEM films were built and further studied. Two were created using PAA and PAH solutions at pH 7.0: PAA 7.0 CL, which had PAA as the outermost layer, and PAH 7.0 CL, which had PAH as the outermost layer. The other two films were made from PAA and PAH solutions at pH 3.5, with PAA (designated PAA 3.5 CL) and PAH (designated PAH 3.5 CL) as the outermost layers, respectively. All samples were thermally cross-linked (CL) in an oven for 2 hours at 180°C. Silicon (100) wafers (10 × 10 mm, CrysTec GmbH, Berlin, Germany) were used as substrates for the ellipsometry and ELISA experiments and glass coverslips (Carl

DOI: https://doi.org/10.26799/cp-sms-nanomed-sensors-egf-2024

Roth GmbH, Karlsruhe, Germany) for the wettability studies and Bradford assay. PEM films were prepared and analyzed at triplicate.

2.2. Thickness

The thickness and refractive indices of PEM films were determined using a Sentech SE800 spectroscopic ellipsometer. Data was evaluated using a four-layer model considering the bulk Si, SiO_2 layer, PEM, and surrounding air.

2.3. Contact angle and surface free energy

Water contact angle (CA) of PEM was measured by sessile drop method using a contact angle goniometer (Dataphysics GmbH, Filderstadt, Germany). Young-Laplace equation was applied to analyze droplet shape. The surface free energy (SFE) of PEMs was analyzed using the Owens, Wendt, Rabel, and Kaelble approach. The surface free tension of deionized water and glycerol were calculated with data from Ström et al. [11] and the surface free tension of n-hexadecane was estimated according to Jasper et al. [12].

3. Protein adsorption

3.1. Bradford assay

A human FNG (Sigma Aldrich-F4883,100 µg/ml) dissolved in phosphate buffered saline (PBS) with pH 7.4 was incubated with PEM-coated substrates for 1 hour at 37°C. The amount of adsorbed FNG was quantified using the Bradford assay [13] by subtracting the concentration of FNG remained in the solution after incubation with PEM coated samples from the initial FNG concentration. UV absorbance measurements were taken using a Lambda Bio+ spectrophotometer (PerkinElmer, Waltham, MA, USA) at 460 nm and 640 nm. A calibration line was used to calculate the amount of adsorbed FNG.

3.2. Indirect ELISA

PEM were preadsorbed with 100% human citrate plasma or FNG (10 µg/mL) solution for 1 hour at 37°C. The amount and conformational state of adsorbed FNG was studied using a modified enzyme immunoassay as previously described [14]. Briefly, monoclonal mouse anti-FNG antibody (Sigma Aldrich, Clone 85D4, 1: 8000) which identifies a conformational sensitive epitope of the □ chain (302– 303) called D-domain, was used to measure the accessibility of this domain for platelet binding. The optical density (OD) was read at 450 nm using a plate reader Infinite F200 PRO (Tecan Trading GmbH, Männedorf, Switzerland).

3.3. Statistical analysis

Statistical analysis was performed using one-way ANOVA with Tukey's post-hoc test to determine significant differences between the various surfaces.

4. Results and discussion

4.1. Physicochemical properties of the PEM films

Thickness of dry PEM was measured (Figure 1 **A**) and showed substantial variations among PEM assembled under different pH conditions, consistent with the findings of Shiratori and Rubner [15]. In acidic pH media (pH 3.5), thicker films (50-55 nm) with higher refractive indices (n≈1.6), therefore higher density were formed, while in neutral pH conditions (pH 7.0), the films tended to be thinner (10-12 nm) and less dense, having lower refractive indices (n≈1.4-1.5). The increase in thickness at lower pH levels can be attributed to reduced ionization and a prevalence of more coiled conformation of the polyelectrolyte chain, especially in the case of PAA [16]. Additionally, film thickness was found to be independent on the type of the outermost layers when both polyelectrolytes are nearly fully charged [15].

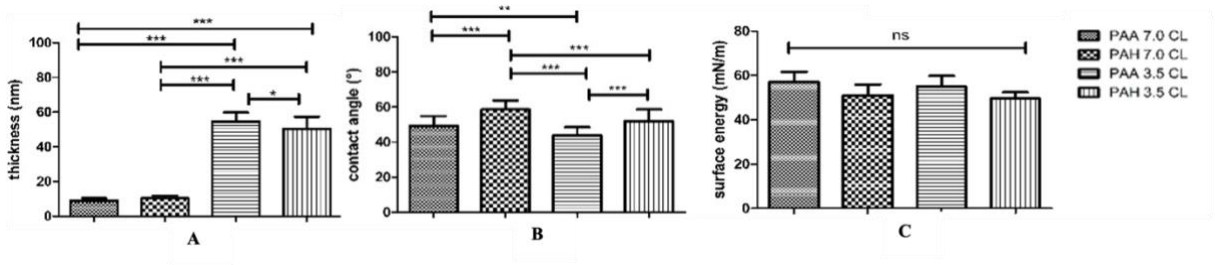

DOI: https://doi.org/10.26799/cp-sms-nanomed-sensors-egf-2024

Figure 1 PEM thickness (A), Contact angle (B) and Surface free Energy (C). ns - non-significant (P > 0.05), * - P ≤ 0.05, ** - P ≤ 0.01, *** - P ≤ 0.001.

All four PAA/PAH films exhibited moderate hydrophilicity with contact angles between 44° and 59° (Figure 1 **B**). The thermal cross-linking of PAA/PAH multilayers likely contributed to this similar hydrophilicity by minimizing the effect of pH on surface properties [17]. The wettability of PAA/PAH multilayers was influenced by the chemical composition of the outermost layer and to a lesser degree, by the assembly pH. PAA-terminated films were generally more hydrophilic than PAH-terminated ones, in line with previous studies [17]. No statistically significant differences in surface free energy were observed among the films (Figure 1 **C**), possibly due to similar levels of dehydration following thermal cross-linking. The assembly pH affects the ionization state, layer thickness and wettability, while the outermost layer determines the overall hydrophilicity.

4.2. Protein adsorption

The colorimetric Bradford assay was applied to measure the total amount of FNG adsorbed to PEM surfaces from a single protein solution (Figure 2 **A**). By this method, maximum adsorption levels were found on the surface of PAA 3.5 CL.

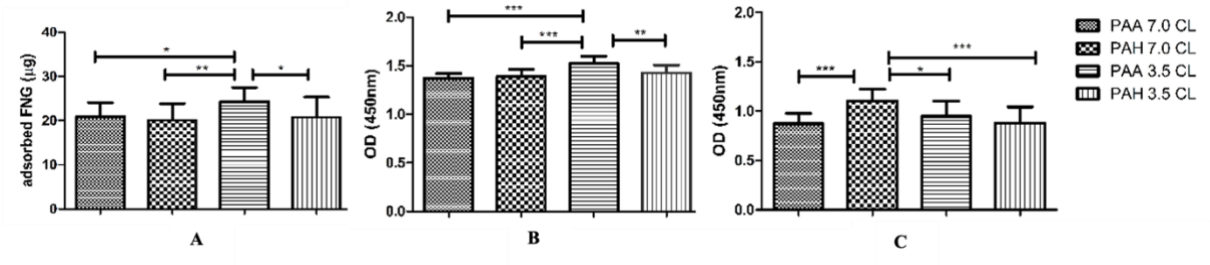

Figure 2 Adsorbed FNG from single solution, assessed by Bradford assay (A), from single solution assessed by ELISA (B) and from human citrate plasma assessed by ELISA (C). ns-non-significant (P > 0.05), * - P ≤ 0.05, ** -P ≤ 0.01, and *** - P ≤ 0.001.

Using the ELISA method (Figure 2 **B** and **C**) we assessed the amount and conformational state of the adsorbed FNG by using a specific antibody against the conformationally sensitive D-domain in the FNG molecule, which is responsible for platelet adhesion [7]. The highest amount of FNG adsorption from single FNG solution as assessed by ELISA was also found on PAA 3.5 CL - the most hydrophilic surface (Figure 2 **B**). However, when adsorbed from human plasma, the highest level of FNG was found on PAH 7.0 CL – the least hydrophilic surface (Figure 2 **C**). The differences in FNG adsorption from single protein solution or plasma are most likely due to the competitive protein adsorption (Vroman effect) from complex protein fluids such as plasma [18]. The protein adsorption mainly correlates with the surface wettability of PEM and the functional groups of the outermost layer, which are the primary parameters contributing to the hydrophilicity. Small changes in contact angle impact the rate of protein adsorption, as also indicated by Vogler [19]. In this way, the outer layer of the PEM can determine the surface wettability and the conformational state of FNG adsorbed from complex protein fluids such as human plasma.

Conclusion

This study highlights the ability of PEM to modulate FNG adsorption on biomaterial surfaces. Surface wettability, primarily influenced by the outermost layer, significantly influences FNG adsorption. The pH of the polyelectrolyte solutions strongly affects the thickness of the films but does not lead to different FNG adsorption. This is most likely due to thermal cross-linking, which minimizes the effect of pH on the surface properties of PEMs.

Acknowledgements

This research was funded by the German Academic Exchange Service (DAAD (Forschungsstipendien - Bi-national betreute Promotionen/Cotutelle, 2023/24 (57645446) and with financial support from the PhD program of Ministry of Education and Science of Bulgaria. We honour Multiprofile Hospital for Active Treatment in Neurology and Psychiatry “St. Naum” in Sofia, Bulgaria for its phlebotomy services.

References

1. H. Hartmann and R. Krastev, "Biofunctionalization of surfaces using polyelectrolyte multilayers “, *BioNanoMaterials*, 18(1-2), 2017.
2. G. Imbir, A. Mzyk, K. Trembecka-Wójciga, E. Jasek-Gajda, H. Plutecka, R. Schirhagl and R. Major, "Polyelectrolyte Multilayer Films Modification with Ag and rGO Influences Platelets Activation and Aggregate Formation under In Vitro Blood Flow “, *Nanomaterials*, 2020.
3. D. Salloum and J. Schlenoff, "Protein Adsorption Modalities on Polyelectrolyte Multilayers “, *Biomacromolecules*, vol. Vol 5/Issue 3, 2004.
4. T. Horbett, "Fibrinogen adsorption to biomaterials “, *J Biomed Mater Res A.,* 2777-2788, 2018.
5. T. Groth, K. Klosz, E. Campbell, R. New and G. Hall B, "Protein adsorption, lymphocyte adhesion and platelet adhesion/activation on polyurethane ureas is related to hard segment content and composition “, *J Biomater Sci Polymer Edn*, vol. 6, p. 497–510, 1994.
6. D. Kiaei, A. Hoffman, T. Horbett and K. Lew, "Platelet and monoclonal antibody binding to fibrinogen adsorbed on glow-discharge-deposited polymers “, *J Biomed Mater Res*, pp. 729-39, 1995.
7. R. Tzoneva, M. Heuchel, T. Groth, G. Altankov, W. Albrecht and D. Paul, "Fibrinogen adsorption and platelet interactions on polymer membranes “, *J Biomater Sci Polym Ed*., pp. 1033-50, 2002.
8. E. Vogler, C. Graper, R. Harper, W. Sugg, M. Lander and J. Brittain, "Contact activation of the plasma coagulation cascade. I. Procoagulant surface chemistry and energy “, *Journal of Biomedical Materials Research*, Vols. Volume 29, Issue 8, 1995.
9. K. Hyltegren, M. Andersson und M. Skepö, „Adsorption of Fibrinogen on Silica Surfaces-The Effect of Attached Nanoparticles”, *Biomolecules*, 2020
10. T. Andreeva, T. Drieschner, D. Golovko, A. Lorenz, K. Rebner and R. Krastev, "Process validation and a new method for quality control of ultrathin polyelectrolyte multilayer coatings “, *Colloids and Surfaces A: Physicochemical and Engineering Aspects*, 2023.
11. G. Ström, "Contact Angles, Work of Adhesion, and Interfacial Tensions at a Dissolving Hydro-carbon Surface “, *Journal of Colloid Interfacial Science* 119 No. 2, p. 352-361, 1987.
12. J. Jasper, E. Kerry and F. Gregorich, "The Orthobaric Surface Tensions and Thermodynamic Properties of the Liquid Surfaces of the n-Alkanes. “, *J. Am. Chem. Soc*., 1953.
13. M. Bradford, "A Rapid and Sensitive Method for the Quantitation of Microgram Quantities of Protein Utilizing the Principle of Protein-Dye Binding “, *Analytical Biochemistry 72*, 248-254, 1976.
14. R. Tzoneva, B. Seifert, W. Albrecht, K. Richau, T. Groth and A. Lendlein, "Hemocompatibility of poly (ether imide) membranes functionalized with carboxylic groups “, J Mater Sci Mater Med 19, 10, 3203-3210, 2008.
15. S. Rubner, S. Shiratori and M.F., "pH-Dependent Thickness Behavior of Sequentially Adsorbed Layers of Weak Polyelectrolytes “, *Macromolecules*, 33, 4213-4219, 2000.
16. S. Burke and C. Barrett, "Controlling the physicochemical properties of weak polyelectrolyte multilayer films through acid/base equilibria*“, *Pure Appl. Chem*., Vol. 76, Nos. 7–8, pp. 1387–1398, 2004.
17. D. Kovačević, T. Klačić., K. Bohinc, "Suppressing the Hofmeister Anion Effect by Thermal Annealing of Thin-Film Multilayers Made of Weak Polyelectrolytes “, *Macromolecules* Vol 55, Issue 21, 2022.
18. L. Vroman, "Effect of Adsorbed Proteins on the Wettability of Hydrophilic and Hydrophobic Solids “, *Nature Letter*, vol. 196, no. https://doi.org/10.1038/196476a0, p. 476–477, 1962.
19. E. Vogler, "Protein adsorption in three dimensions “, *Biomaterials*, volume 33, Issue 5, 2012.

Proceedings of the NanoMed 2024 International Conference
Barcelona, Spain, 23 – 25 October 2024
DOI: https://doi.org/10.26799/cp-sms-nanomed-sensors-egf-2024

Advanced Biomaterials for Biomedical Applications: Alginate-Gelatine Hydrogels with ICG Delivery

Antonio de Nigris [1], Giuseppe Quero [2], Giuseppe Peter Vanoli [1], Luigi Ambrosone [1]

[1] University of Molise, Department of Medicine and Health Sciences, 86100 Campobasso, Italy, a.denigris1@studenti.unimol.it, giuseppe.vanoli@unimol.it, ambroson@unimol.it
[2] University of Molise, Department of Bioscience and Territory, 8090 Pesche (IS), Italy, giuseppe.quero@unimol.it

Abstract

Three types of patches, such as Sodium Alginate/Gelatin, Sodium Alginate/Gelatin/Free Indocyanine Green and Alginate/Gelatin/Liposomes containing Indocyanine Green were bioprinted, non-crosslinked and chemo-physically characterized. Investigation via Atomic Force Microscopy (AFM) reveals that the surfaces have little roughness and few voids. The dye-laden liposomal dispersion can be exploited to modulate the release rate. Preliminary evidence indicates that the interfacial turbulence generated by liposomes disruption enhances dye/drug release.

Keywords: hydrogels, patches, liposomes, bioprinting, indocyanine green.

1. Introduction

The development of advanced biomaterials is a critical area of research, particularly for applications such as tissue engineering, wound healing, and drug delivery [1]. Among the promising candidates for these applications are hydrogels composed of alginate and gelatine [2]. These materials offer a combination of biocompatibility, biodegradability, and mechanical tunability, making them ideal for creating resorbable patches and scaffolds. In this report, we explore the development and potential applications of three distinct types of alginate-gelatine hydrogels, each designed to deliver indocyanine green (ICG), a fluorescent dye commonly used in medical imaging [3]. The base material is a hydrogel composed of alginate and porcine gelatine with a high Bloom value of 300. Alginate, a naturally occurring polysaccharide, forms stable hydrogels in the presence of divalent cations like calcium ions [4]. Gelatine, derived from collagen, enhances the mechanical properties of the hydrogel and introduces cell-adhesive sequences that promote cellular attachment and proliferation [5]. A biodegradable dye releasing device would assist medical image analysis to visualize and protect tissues in real-time. Another perspective explored by drug eluting patches is the possibility to deliver therapeutic agents directly to the target tissue, which could significantly improve outcomes of wound healing, cancer treatment [6] and impaired tissue regeneration processes.

In non-crosslinked hydrogels, the polymer chains are not chemically bonded together, which results in a more flexible and less structured network. This lack of crosslinking typically means there are fewer or no permanent pores formed within the gel matrix [7]. The absence of crosslinking reduces the formation of pores on the surface, which can lead to a smoother hydrogel surface. This might be beneficial in applications where a uniform surface is desired. The lack of a tightly crosslinked network facilitates the diffusion of small molecules, like ICG or other drugs, out of the hydrogel. Since the polymer chains are not strongly bound together, there are more pathways for the encapsulated substances to move through and eventually diffuse out of the gel. In contrast, a crosslinked hydrogel would have a more defined network, which could restrict the movement of molecules within the gel, thereby slowing down the release of encapsulated substances. However, this also means that the release might be less controlled and could happen more rapidly in a non-crosslinked system. In the latter hydrogels, the modulation of diffusion and erosion properties, such as for ICG release and the biodegradability of bioprinted patches, can be achieved through several strategies, even without chemical crosslinking. In summary, even without crosslinking, the diffusion of ICG and the erosion rate of the bioprinted patch can be modulated by altering the hydrogel composition, structure, and environmental interactions. These approaches allow for tailored release profiles and degradation rates suitable for various biomedical applications.

DOI: https://doi.org/10.26799/cp-sms-nanomed-sensors-egf-2024

2. Preparation of hydrogels and bioprinting of patches

Sodium alginate (NaAlg) powder was mixed with UPW pre-heated at 80°C and the resulting mixture was kept under rigorous stirring (125 rpm) until a homogeneous solution (5.7% w/v) was obtained. Separately, a 3.8% (w/v) aqueous solution of gelatin (Gel) was prepared by mixing gelatin in UPW pre-heated to 60°C and stirred for 45 min. Then, both solutions were mixed and kept at 80°C under vigorous stirring for 15 min to achieve complete homogeneity. This formulation forms the hydrogel base, B_0. In order to prepare a colored patch, 1 ml of 5 $mgml^{-1}$ ICG solution was added to the freshly prepared B_0 system and kept under agitation for 15 min at room temperature. This formulation forms the hydrogel B_1.

Liposomal dispersions containing dye were prepared by dissolving 1 ml of 5 $mgml^{-1}$ ICG solution at room temperature in the aqueous phase during preparation. Then, gel was prepared by adding a volume of 0.5 ml of the resulting dispersion to the freshly prepared B0 system and kept under agitation for 15 min. This formulation forms the hydrogel B_2. Liposomes were prepared from phosphatidylcholine by the well-known reverse-phase method [8]. Mean particle size and particle size distribution of the liposome dispersions were evaluated by DLS using a Zetasizer Nano ZS (Malvern Instruments Ltd., Worcestershire, UK). Formulations were measured at room temperature and processed with the Zetasizer Software (research grade; Malvern Panalytical, UK) using default values for all analysis. Hydrodynamic diameter Z_{avg} = (134 ± 9) nm (sphere-equivalent scattered light intensity-weighted harmonic average hydrodynamic diameter) and polydispersity index (PdI = 0.051) determined by cumulants analysis were the primary size and size distribution measurands and were used as a reference size for other samples [9]. All patches, drawn with Autodesk Inventor Pro software as a square-based parallelepiped with a side of 10 mm and a height of 0.4 mm, were manufactured by a BIOX Bioprinter (CELLINK-Twin Helix). The final height of the artifact (0.4 mm) was obtained by deposition of two layers of material using conical bioprinting nozzles (27 gauge) and operating at printhead temperature of 37°C, pressure of 50 kPa, velocity of 5.0 mms^{-1}, preflow of 100 ms and printbed temperature 25°C. The bioprinting process was carried out in 90 mm diameter plastic Petri dishes. The samples subjected to surface investigations were manufactured on borosilcate glass slides (Fig.1). The fresh bioprinted patches were left air-drying for 48 hours. The dyed patches were also shielded from natural light to avoid indocyanine green photodeterioration [10].

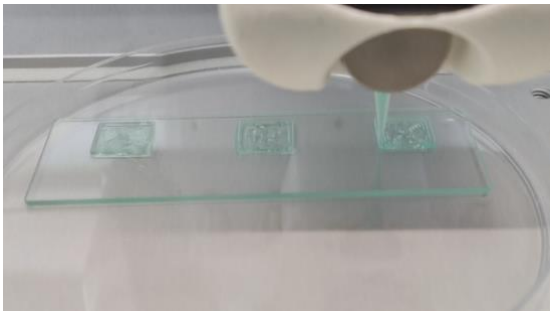

Fig. 1: Bioprinting of patches containing ICG.

3. Results and discussion

The bioprinted patches PB_0, PB_1 and PB_2 exhibit different surface properties, as shown in Fig. 2. The surfaces are sufficiently smooth and have no pores.

DOI: https://doi.org/10.26799/cp-sms-nanomed-sensors-egf-2024

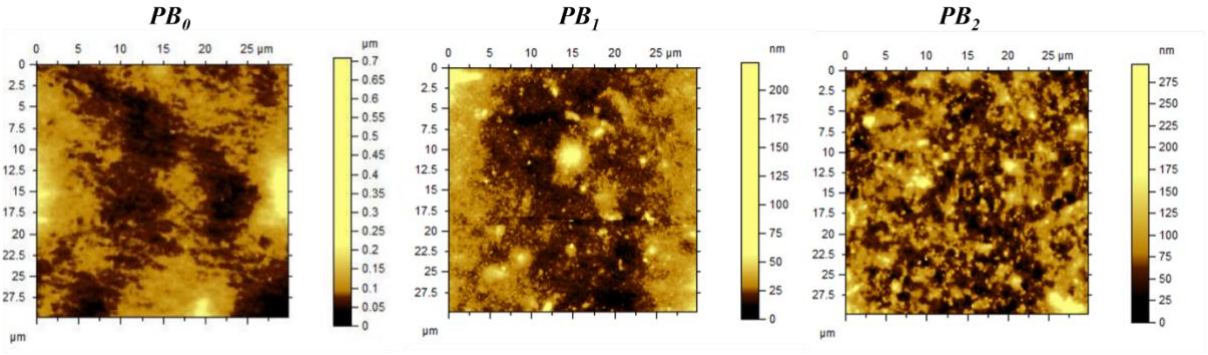

Fig. 2: AFM images on 0.03 x 0.03 mm^{-2} spots on the surfaces of the three different patches.

AFM analysis indicated that the surface of the gels lacks significant in porosity, but with increasing complexity, such as with liposome incorporation, surface roughness increases. The distribution of liposomes sizes in the hydrogel matches the primary dispersion, indicating that liposomes remain intact after embedding, which is crucial for maintaining controlled release e properties.

AFM images shows that all patches (PB_0 - base hydrogel, PB_1 - hydrogel with free ICG, and PB_2 - hydrogel with liposomal ICG) maintain a non-porous surface. This absence of surface pores helps regulate the release of encapsulated materials, preventing rapid leakage and supporting a more controlled release profile. The surface height increases slightly from PB_0 to PB_1 and PB_2, with the liposome-containing hydrogel (PB_2) showing an asymmetrical height distribution. This indicates that the liposomes are well-incorporated within the matrix without disturbing the overall surface structure.

The non-crosslinked hydrogels allow the diffusion of ICG or other drugs. The incorporation of liposomal ICG provides an advantage over free ICG by offering a more sustained release due to the protective liposomal encapsulation. The release of ICG from the liposomal hydrogel can be further controlled by adjusting the lipid composition of the liposomes or altering the properties of the hydrogel matrix itself.

The absence of crosslinking also affects the erosion rate of the patch. A faster erosion rate might result in quicker drug release, while slower erosion ensures a prolonged therapeutic effect. This erodibility can be tuned by modifying the balance between alginate and gelatin concentrations or by introducing other stabilizing agents. Thus, the composition of the patch plays a crucial role in both the release kinetics of ICG and the overall degradation time, which are critical factors in the design of resorbable patches for medical applications. The ability to modify the liposomal encapsulation also opens up the possibility of creating stimuli-responsive systems, where the release of ICG or other drugs can be triggered by environmental factors such as pH or temperature.

4. Conclusion

The combination of alginate-gelatin hydrogels with ICG, both free and encapsulated in liposomes, forms a versatile system for creating bioprinted, resorbable and drug eluting patches. The key findings and their implications for the application of these patches are many. On the one hand these bioprinted devices can be applied in various biomedical fields, especially in wound healing, localized drug delivery, oncology or diagnostics. On the other hand, by fine-tuning the hydrogel formulation and by engineering the pathc-tissue interaction at the nanoscale, the release of therapeutic agents can be programmed to meet specific clinical needs. The flexibility in the design of these patches and the versatile manufacturing process make them suitable for personalized medicine approaches, where patient-specific factors could dictate the exact composition and release profile of the drug-loaded patch. This synthesis provides an overview of how these hydrogel-based patches can be developed and optimized for controlled drug release and specific therapeutic applications.

DOI: https://doi.org/10.26799/cp-sms-nanomed-sensors-egf-2024

References

1. M.A. Samp, N. C. Iovanac, and A. J. Nolte. "*Biomaterials Science & Engineering*", vol. 3, pp. 3176-3182, 2017.
2. T. Biswal, S. K. BadJena and D. Pradhan. "Sustainable biomaterials and their applications: a short review", *Materials Today*, vol. 30, no. 2, pp 272-282, 2020.
3. A, G. Podoleanu, G. M. Dobre, R. Cernat, J. A. Rogers, P. Justin, R. B. Rosen, P. Garcia. "Investigations of the eye fundus using a simultaneous optical coherence tomography/indocyanine green fluorescence imaging system", *Journal of Biomedical Optics*, vol. 12, no. 1, 2007.
4. W. Mackie, R. Noy and D.B. Sellen. "Solution properties of sodium alginate", *Biopolymers*, vol. 19, pp. 1839-1860, 1980.
5. S.C Wu, W.H. Chang, G.C. Dong, K.Y. Chen, Y.S Chen, C.H. Yao. "Cell adhesion and proliferation enhancement by gelatin nanofiber scaffolds". *Journal of Bioactive and Compatible Polymers*, vol. 26, no. 6, pp 565-577, 2011.
6. G. Sharma, S. Anabousi, C. Ehrhardt. "Liposomes as targeted drug delivery systems in the treatment of breast cancer", *Journal of Drug Targeting,* vol. 14, no. 6, pp 301-310, 2008.
7. B. P. Santora, M. R. Gagné, K. G. Moloy, N. S. Radu. "Porogen and Cross-Linking Effects on the Surface Area, Pore Volume Distribution, and Morphology of Macroporous Polymers Obtained by Bulk Polymerization", *Macromolecules*, vol. 34, no. 3, pp 658-661, 2001.
8. F. Skoda Jr, D. Papahadjopuulos. "Comparative properties and methods of preparation of lipid vesicles (liposomes)," *Annual review of biophysics and bioengineering*, vol. 9, pp. 467-508, 1980.
9. G. Cinelli, G. Bufalo, F. Lopez and L. Ambrosone "Cooperativity between dimerization and binding equilibria in the ternary system laponite-indocyanine green-water", *ChemEngineering* vol. 5, no. 5, 2020, https://doi.org/10.3390/chemengineering5010006.
10. E. Engel, R. Schraml, T. Maisch, K. Kobuch, B. König, R.M. Szeimies, J. Hillenkamp, W. Bäumler, R. Vasold. "Light-Induced Decomposition of Indocyanine Green", *Investigative ophthalmology & visual science*, vol. 49, no. 5, pp 1777-1783, 2008.

Proceedings of the Sensors 2024 International Conference
Barcelona, Spain, 23 – 25 October 2024
DOI: https://doi.org/10.26799/cp-sms-nanomed-sensors-egf-2024

Smart Patch for Continuous Monitoring and Stretchable Electronics in Enhancing Patient Outcomes

Alejandra Ben-Aissa, Martina Moreno, Brenda Molina, Marc Alique, Ana Moya

Eurecat, Centre Tecnològic de Catalunya, Functional Printing and Embedded Devices Unit,
Av. Ernest Lluch, 36 Mataró, Spain, alejandra.benaissa@eurecat.org

Abstract

The management of critically ill patients within Intensive Care Units (ICUs) represents a great challenge to global healthcare and requires a paradigm shift towards vigilant and continuous monitoring to optimize clinical decision-making and improve outcomes. Due to the dynamic nature of patients' conditions in these settings, the limitations of intermittent monitoring systems are highlighted. The potential consequences of inadequate monitoring, including delayed recognition of deteriorating conditions and suboptimal utilization of healthcare resources emphasize the need for real-time, comprehensive data to guide timely interventions and prevent adverse events. The integration of advanced sensors, wearable devices, and data analytics empower healthcare professionals with the ability to continuously track vital signs, physiological parameters, and other critical metrics. This constant stream of data facilitates early detection of subtle changes in a patient's condition, enabling proactive interventions and personalized care plans tailored to individual needs. The development of these recent wearable devices has been influenced by printed electronics (PE), known for its ability to create flexible devices on diverse stretchable substrates using innovative printable materials. These wearables can be made on materials like thermoplastic polyurethanes (TPU), enabling integration into textiles and facilitating human-skin interaction. Herein, in this study, we harness the potential of PE for medical applications, specifically displaying a fully integrated non-invasive wearable designed for the early detection of sepsis in ICU patients. Our approach includes electrochemical biosensors for the continuous monitoring of glucose and lactate concentrations in sweat, which provide real-time data on the patient's energy metabolism reflecting cellular dysfunction and its monitorization might prevent or revert the fatal metabolic dysregulation in septic patients. This research underscores the transformative potential of stretchable electronics and innovative materials, offering a flexible biosensor platform that transcends traditional medical applications allowing personalized interventions for optimal management.

Keywords: Printed Electronics (PE), Wearable Biosensors, Glucose and Lactate Monitoring, Intensive Care Units (ICU)

1. Introduction

Managing critically ill patients in Intensive Care Units (ICUs) is a cornerstone challenge in modern healthcare, necessitating constant vigilance and innovation. The dynamic nature of patients' conditions in these settings highlights the limitations of traditional, intermittent monitoring systems, which often fail to detect critical changes in real time [1]. Moreover, laboratory-based techniques—dependent on delayed sample transport, analysis, and reporting—cannot meet the demands for rapid and accurate decision-making. Addressing this gap, printed electronics (PE) has emerged as a transformative technology, offering a cost-effective, scalable, and highly versatile platform for developing advanced wearable devices that enable continuous monitoring directly at the bedside.

Printed electronics stands out for its unique ability to combine low-cost manufacturing with extraordinary versatility, making it a disruptive force in healthcare technology. By leveraging innovative printable materials and processes such as roll-to-roll printing, PE enables the mass production of sophisticated devices at significantly reduced costs, breaking down economic barriers to widespread adoption [2]. Beyond affordability, the flexibility of PE allows for seamless integration into unconventional substrates, including stretchable materials like thermoplastic polyurethanes (TPUs) that conform to irregular surfaces [3]. This adaptability facilitates the creation of wearables that are not only lightweight and comfortable but also capable of adhering naturally to the human body, offering continuous monitoring without restricting movement. Furthermore, its scalable nature ensures that production can quickly respond to high demand, meeting the needs of global healthcare systems. Importantly, the inherent design flexibility of PE allows for customization, enabling devices to take on various shapes and functionalities tailored to specific clinical requirements, such as biosensors

DOI: https://doi.org/10.26799/cp-sms-nanomed-sensors-egf-2024

embedded in autonomous patches for ICU patients. With the ability to integrate components for sensing, data processing, communication, and display, printed electronics empowers the creation of multifunctional, portable systems that redefine the possibilities of real-time health monitoring.

These unique attributes of PE have enabled the development of advanced wearable biosensors designed for non-invasive monitoring of critical biomarkers, such as glucose and lactate, in sweat. Sweat, as a biofluid, offers several key advantages: it can be sampled non-invasively, is abundant, and provides essential biochemical information about metabolic and physiological states. This makes it an ideal medium for real-time detection of conditions such as sepsis, where early intervention is crucial for patient survival.

The next generation of wearable devices is guided by the REASSURED framework, prioritizing affordability, reliability, and ease of use [4]. To meet these requirements, an effective wearable biosensor platform must integrate several functional components: actuation and control modules for enhanced usability, microfluidics for precise sample handling, and advanced electronics for data automation and sensitivity. Furthermore, these devices must include intuitive display systems to communicate results directly, energy storage solutions for autonomous operation, and connectivity features for remote data transmission and storage. Most critically, high-specificity and high-sensitivity sensors are essential to detect subtle physiological changes and provide timely, accurate diagnostic information [5].

In this study, we showcase the application of PE in designing a cutting-edge wearable biosensor platform for ICU patients. This device integrates electrochemical biosensors for the continuous measurement of glucose and lactate in sweat, providing real-time insights into cellular dysfunction and energy metabolism. By detecting early signs of sepsis, this system empowers healthcare providers to implement timely and personalized interventions, potentially saving lives and reducing ICU costs.

The flexibility, scalability, and affordability of printed electronics represent a paradigm shift in healthcare technology. By bridging the gap between traditional lab-based systems and real-time continuous monitoring, PE-based devices have the potential to revolutionize critical care, ensuring better outcomes for patients worldwide

2. Materials and Methods

2.1. Screen-printed electrodes

The flexible electrodes were fabricated using screen-printing technology, with thermoplastic polyurethane (TPU) serving as the substrate. TPU was chosen due to its stretchable and flexible properties, making it ideal for wearable applications. The inks employed for the printing process were specifically designed for compatibility with flexible substrates, ensuring durability and reliable performance under dynamic conditions.

The flexible electrodes were fabricated using screen-printing technology, with thermoplastic polyurethane (TPU) as the substrate. TPU was selected for its stretchable and flexible properties, making it ideal for wearable applications. The inks used in the printing process were designed for compatibility with flexible substrates, ensuring reliable and durable performance.

The fabrication process of the electrodes followed a meticulous sequence of screen-printing steps to achieve a multi-layered structure. The process began with the preparation of the substrate, using thermoplastic polyurethane (TPU) as the base material. TPU was chosen for its mechanical flexibility and suitability for wearable applications.

The first step in electrode fabrication involved printing conductive tracks using silver ink to establish the electrical pathways. Subsequently, the reference electrode was created by applying a layer of silver/silver chloride (Ag/AgCl) ink. This electrode plays a crucial role in maintaining a stable baseline potential during electrochemical reactions.

Next, the working electrode was printed using carbon ink, enhanced with Prussian blue as a mediator to improve its sensitivity to changes in the analyte. The counter electrode, essential for ensuring efficient electron flow during the electrochemical process, was also printed with carbon ink.

To finalize the structure, a protective dielectric layer was applied. This layer served to shield specific parts of the sensor from exposure to the solution, ensuring that only the functional areas of the electrodes remained in

DOI: https://doi.org/10.26799/cp-sms-nanomed-sensors-egf-2024

contact with the analyte. This precise fabrication method resulted in a robust and flexible electrochemical system suitable for continuous monitoring applications (Figure 1).

Fig. 1: Schematic representation of the different printed layers in TPU and the resulting screen-printed electrode

2.2. Enzymatic membranes

The lactate and glucose membranes were deposited onto each of the working electrodes using an automated drop-casting procedure to ensure precision and consistency. These membranes were composed of the respective enzymes, glucose oxidase or lactate oxidase, bovine serum albumin (BSA), and glutaraldehyde. After deposition, the membranes were cured at room temperature for 2 hours to stabilize their structure and ensure proper adhesion.

2.3. Electrochemical characterization

The electrochemical characterization of the printed sensors was carried out to evaluate their performance and select the optimal operating potential. The potential was determined using cyclic voltammetry (CV), ensuring sensitivity and specificity for the target analytes. Chronoamperometric measurements were then performed at -0,2V, the selected potential to monitor the sensor's response over time. Calibration curves were generated for each analyte by testing a range of concentrations (0, 1, 2, 5, and 10 mM) in artificial sweat. The artificial sweat had a composition designed to mimic physiological conditions, containing 85 mM NaCl, 13 mM KCl, and 15 mM urea (EN1811:201219).

2.4. Selectivity study

An interference study was performed to evaluate the specificity of the sensors for glucose and lactate in the presence of common interferents found in sweat. According to the literature, the most relevant interferents for lactate detection are glucose, urea, and ascorbic acid, while for glucose detection, they are lactate, urea, and ascorbic acid. To investigate this, different concentrations of these interferents were added to 5 mM glucose solutions to examine their impact on the glucose sensor's response. A similar procedure was followed for the lactate sensor, using 5 mM lactate solutions.

3. Results and discussion

The results obtained from the amperometric calibration curves for the glucose and lactate sensors demonstrate their analytical performance across different concentrations of the analytes (Figure 2). For the glucose sensor, the limit of detection (LOD) was determined to be 0.91 mM and a detection range spanning from 0 to 10 mM. Similarly, the lactate sensor showed a LOD of 1.54 mM, and the same detection range of 0 to 10 mM. These parameters indicate the suitability of both sensors for detecting physiological concentrations of glucose and lactate, aligning with typical ranges observed in sweat.

DOI: https://doi.org/10.26799/cp-sms-nanomed-sensors-egf-2024

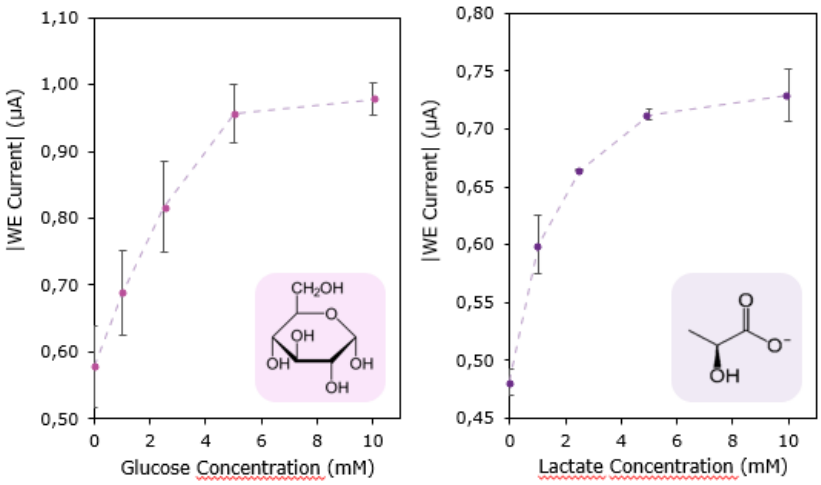

Fig. 2: Amperometric calibration curves for the glucose and lactate sensors obtained by measuring current responses at -0,2V.

Regarding the interference study, the results clearly demonstrate that there is no significant interference affecting the glucose sensor. The relative current response remains consistent even in the presence of potential interferents such as lactate, urea, and ascorbic acid. This indicates that the glucose sensor maintains its specificity and reliability, effectively distinguishing glucose from other compounds commonly found in sweat. Similarly, no noticeable differences in the sensor response were observed when varying the concentration of interferents while keeping a constant lactate concentration. The relative current remained stable, indicating that the lactate sensor is not significantly affected by the presence of common interferents such as glucose, urea, and ascorbic acid, demonstrating its robustness and selectivity in detecting lactate (Figure 3).

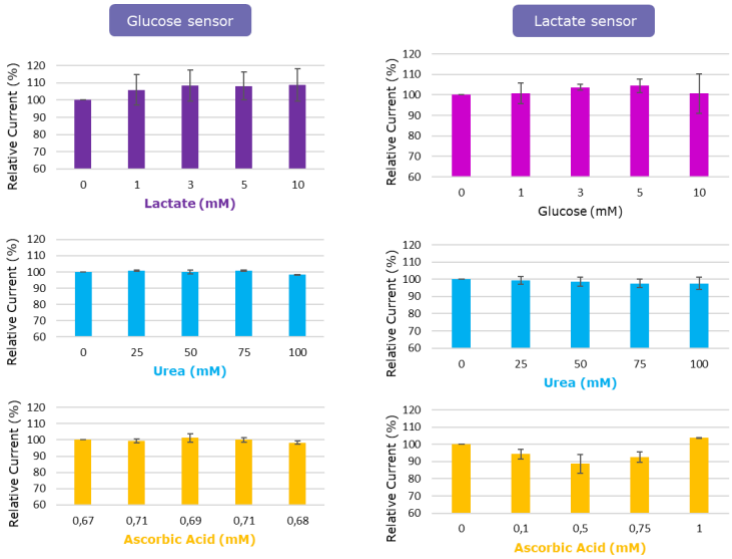

Fig. 3: Interference study results for the glucose and lactate sensors. The graphs show the relative current responses of the glucose sensor (left) and lactate sensor (right) when various concentrations of interferents (lactate/glucose, urea, and ascorbic acid) were added to solutions with a constant concentration of glucose (5 mM) and lactate (5 mM), respectively.

4. Conclusion

In conclusion, this study demonstrates the potential of printed electronics (PE) in developing non-invasive wearable biosensors for continuous monitoring of glucose and lactate levels in sweat, offering a promising solution for real-time patient care, particularly in ICU settings. The glucose and lactate sensors exhibit excellent performance, with well-defined limits of detection, reliable amperometric responses, and robust selectivity, as evidenced by the interference studies. The results highlight the sensors' capability to accurately detect physiological concentrations of these biomarkers, unaffected by common interferents such as glucose, lactate, urea, and ascorbic acid.

DOI: https://doi.org/10.26799/cp-sms-nanomed-sensors-egf-2024

Despite the significant progress made, there are still critical steps to be taken for full clinical validation. Moving forward, it will be essential to quantify these parameters with real sweat samples to confirm the sensors' accuracy and performance in more complex biological fluids. Additionally, a bioequivalence study will be conducted to compare the sensor readings with blood concentrations of glucose and lactate, further validating the wearable biosensors as viable alternatives for non-invasive monitoring. Although substantial advancements have been made, these future steps will be crucial in overcoming existing challenges and ensuring the clinical applicability of these devices for personalized and continuous healthcare management.

Acknowledgements

This work was financially supported by the Catalan Government through the funding grant ACCIÓ-Eurecat (Project Flagship- BeOnSkin).

References

1. S. Bailly, G. Meyfroidt, and J. F. Timsit, "What's new in ICU in 2020: Critical care for today and tomorrow," Intensive Care Medicine, vol. 46, no. 10, pp. 1882–1890, 2020.
2. M. J. Nunes et al., "Screen-Printed Electrodes Testing for Detection of Potential Stress Biomarkers in Sweat," Electrocatalysis, vol. 13, 2022, doi: 10.1007/s12678-022-00709-7.
3. M. Alique et al., "Multiplex Sensing Electronic Skin Based on Seamless Fully Printed Stretchable Piezoelectric Devices," Advanced Sensor Research, vol. 2, 2022, doi: 10.1002/adsr.202200016.
4. K. J. Land, D. I. Boeras, X. S. Chen et al., "REASSURED diagnostics to inform disease control strategies, strengthen health systems and improve patient outcomes," Nature Microbiology, vol. 4, pp. 46–54, 2019, doi: 10.1038/s41564-018-0295-3.
5. S. Smith, J. G. Korvink, D. Mager, and K. Land, "The potential of paper-based diagnostics to meet the ASSURED criteria," RSC Advances, Issue 59, 2018.

Proceedings of the Sensors 2024 International Conference
Barcelona, Spain, 23 – 25 October 2024
DOI: https://doi.org/10.26799/cp-sms-nanomed-sensors-egf-2024

Experimental Investigation of Thermal Tuning for Laterally Excited Bulk Acoustic Wave MEMS Resonators using SOI Bulk Heating

Munira Bengashier, Owen Casha, Ivan Grech, Russell Farrugia, Joseph Micallef and Edward Gatt

Department of Microelectronics and Nanoelectronics
University of Malta, Msida, Malta, munira.bengashier.15@um.edu.mt

Abstract

This paper presents the experimental investigation of electrothermal fine frequency tuning for a 60 MHz laterally excited contour mode bulk acoustic wave MEMS resonator, fabricated using the PiezoMUMPs multi-process wafer process. Tuning is achieved via electrothermal SOI bulk heating of the resonator, so that its resonant frequency is shifted by inducing additional stresses in the device, as well as varying its elastic properties via a temperature change. Experimental results show that the resonant frequency decreases with an increase in the electrical heating power, which is applied to the resonator SOI bulk via two heating electrodes. For a 50-mW heating power swing, the resonator frequency varies from 61.368 MHz to 61.418 MHz. Measured results show that the SOI bulk resistance remains approximately constant over this tuning range, with a value of around 31 Ω. The discussion of the experimental results is aided and confirmed via finite element modelling and simulation.

Keywords: thermal tuning, SOI bulk heating, LBAW resonators, PiezoMUMPs, MEMS.

1. Introduction

Lateral-mode MEMS resonators employing piezoelectric actuation, have been successfully implemented within applications including filters and frequency synthesizers, as a replacement of the quartz crystal component. Such MEMS components were effectively integrated within low power and low phase noise oscillators [1,2,3]. The shift in the resonant frequency due to environmental conditions such as temperature and pressure variations, or fabrication process tolerances, such as those due to geometrical dimensions and material properties variations, is still considered to be a drawback for MEMS resonators [4]. Therefore, the capability to fine tuning the frequency of a resonator is critical in several high precision applications [1, 5].

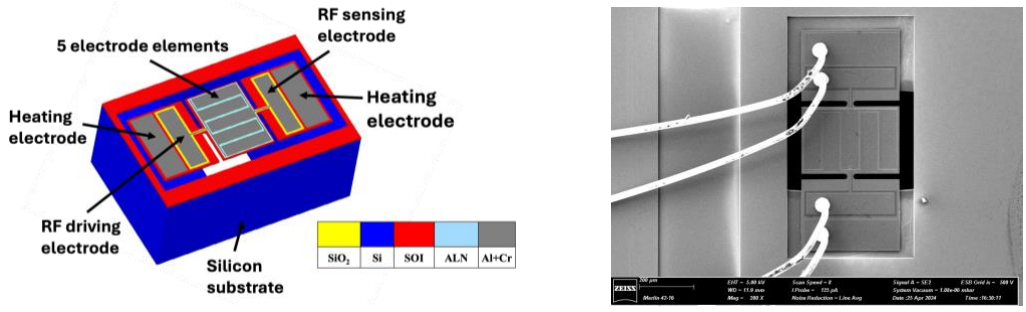

(a) (b)

Fig. 1: (a) Simplified diagram of the LBAW rectangular resonator including the pads used for electro-thermal tuning (b) Micrograph of the fabricated LBAW PiezoMUMPs resonator including two electro-thermal heating electrodes.

This paper presents the experimental investigation of electrothermal fine frequency tuning for a 60 MHz laterally excited contour mode bulk acoustic wave (LBAW) MEMS resonator, fabricated using the PiezoMUMPs multi-process wafer process, which consists of a 0.5 µm Aluminium Nitride (AlN) piezoelectric material layer over a silicon-on-insulator (SOI) structure having a thickness of 10 µm (Fig. 1a). Tuning is achieved via electrothermal SOI bulk heating of the resonator, so that its resonant frequency is shifted by inducing additional stresses in the device, as well as varying its elastic properties via a temperature change. While this paper focuses on the application of SOI bulk heating to MEMS resonators, the same heating principle can be employed in other applications, such as the calibration or resetting of MEMS gas sensors based on resonators coated with a functionalised layer. Fig. 1(b) presents a micrograph of the fabricated five piezoelectric element LBAW PiezoMUMPs resonator. It includes two metal heating electrodes positioned directly over the

Proceedings of the Sensors 2024 International Conference
Barcelona, Spain, 23 – 25 October 2024
DOI: https://doi.org/10.26799/cp-sms-nanomed-sensors-egf-2024

SOI layer islands located on both sides of the resonator, enabling a heating current to be applied through bonding wires. Two sensing metal electrodes with an oxide layer beneath them, allow the measurement of the transmission scattering parameter S_{21} via a vector network analyser. This setup generates electrothermal power, heating the SOI layer and transferring the heat to the resonator body through the tethers.

2. PiezoMUMPs Process

A cross-sectional view presenting all the layers of the PiezoMUMPs process and their respective thickness in µm, is shown in Fig. 3 [6]. It is a five-mask process commencing from a 150 mm diameter SOI wafer featuring a silicon thickness of 10±1 µm, an oxide thickness of 1±0.05 µm, and a handle wafer (substrate) thickness of 400±5 µm.

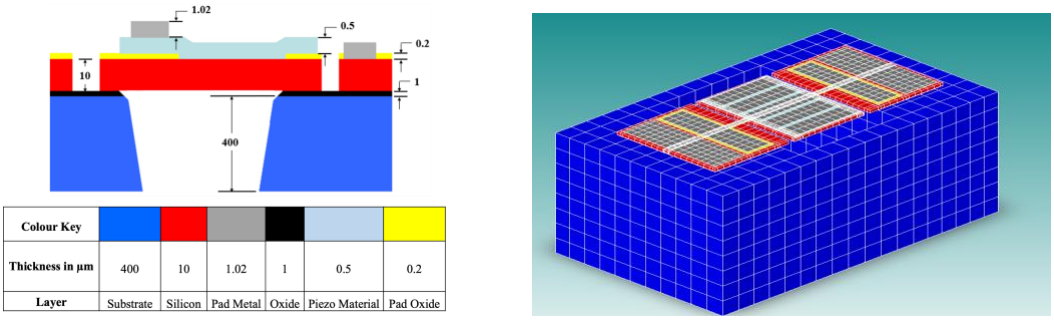

(a) (b)

Fig. 3: (a) Cross sectional view of the PiezoMUMPs process including the various layers and their thickness in µm [6] (b) 3D view of the finite element (FE) resonator model implemented in CoventorMP using a 20 µm Manhattan brick mesh for the resonator and a 30 µm Manhattan brick mesh for the silicon substrate.

The process commences with the doping of the silicon layer, which is then patterned and etched down to the oxide layer; these two layers act as a mechanical structure. The substrate can also be patterned and etched from the bottom side to the oxide layer. After that, the thermal oxide layer is patterned and etched in order to provide isolation between the SOI layer and the AlN and pad metal layers. The pad metal is deposited via a lift-off process and consists of 20 nm of chromium and 1 µm of aluminium [6].

3. Resonator Measured and Simulation Results

In order to vary the heating current, a voltage source of 9 V and a 15 kΩ variable resistor connected in series with the heating electrodes of the fabricated resonator prototype were used. The measured transmission magnitude plots for different heating currents are shown in Fig. 4.

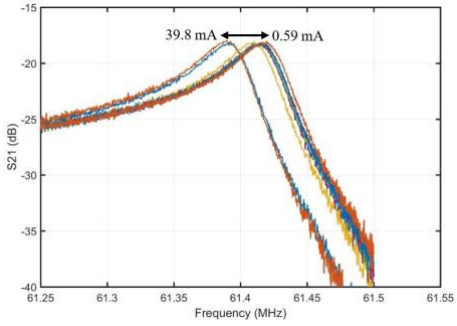

Fig. 4: Measured variation of the frequency response of the resonator transmission gain $|S_{21}|$ with the heating element current.

These experimental results show that the resonant frequency decreases with an increase in the electrical heating power applied to the resonator SOI bulk via the two heating electrodes. For a 50-mW heating power swing, the resonator frequency varies from 61.368 MHz to 61.418 MHz, as shown in Fig. 5. The measured 5th mode resonator frequency variation was confirmed via a finite element (FE) simulation model (refer to Fig 3b) implemented using CoventorMP while considering the electrothermal material properties listed in Table 1.

DOI: https://doi.org/10.26799/cp-sms-nanomed-sensors-egf-2024

Table 1: Electrothermal material properties used in the FE simulation model of the resonator

Layer	Electric Conductivity (pS/µm)	Thermal Conductivity (pW/µm.K)
Substrate	$1x10^{7}$	$1.57x10^{8}$
SOI	$2x10^{10}$	$1.48x10^{8}$
SiO_2	0.0001	$1.42x10^{6}$

Even though the FE simulation model gave a similar variation in frequency, the nominal resonator frequency is around 4 MHz lower than the measured value due to process related variations. An electrothermal simulation was first carried out using the CoventorMP MemMech module to obtain the variation of both the resonator temperature and the heating current with the applied voltage, while assuming a fixed temperature of 300 K on the outer surface of the substrate as a boundary condition. Then a modal analysis was performed on the resonator without the substrate, to obtain the variation of the 5th mode resonant frequency with an SOI temperature change from 300 K to 320 K. A temperature trajectory was applied on the SOI top surface (red layer with respect to Fig. 3b) while fixing all the other sides. The temperature dependence of the Young's modulus E in MPa of the SOI layer was modelled via a polynomial (E=-12.9T+1.69760x10^{5}), where T is the temperature in Kelvin [7, 8]. A Poisson ratio value of 0.29 was considered. The simulation results were then combined to obtain the behaviour shown in Fig. 5.

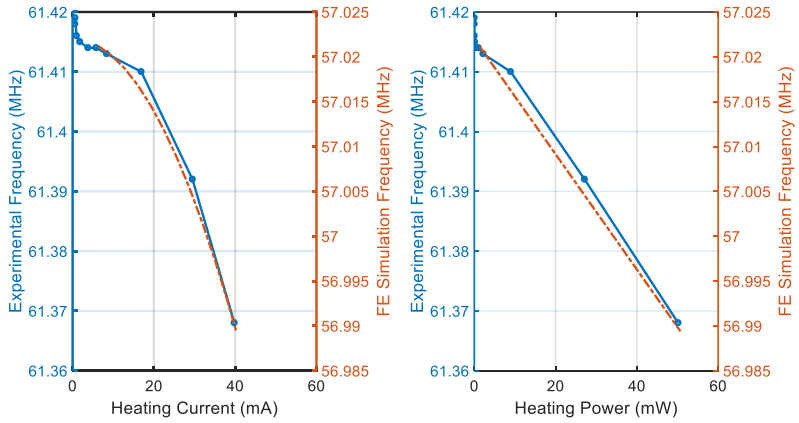

Fig. 5: Measured and simulated variation of the resonator frequency with the heating element current and power.

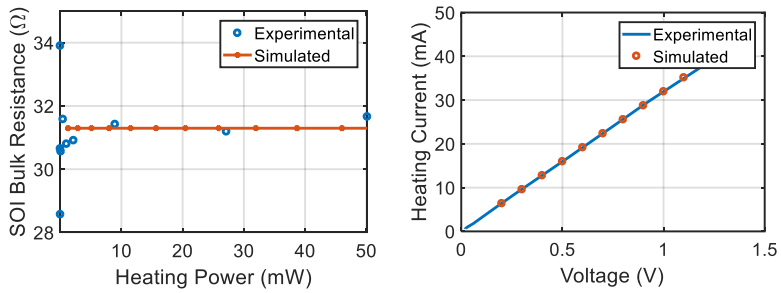

Fig. 6: (a) Variation of the SOI bulk resistance for the measured resonator prototype and the simulated resonator model (b) Variation of the heating current with the applied voltage for both the measured resonator prototype and its FE simulated model.

Measured results show that the SOI bulk resistance remains approximately constant over this tuning range, with a value of around 31 Ω. This was also confirmed via the FE simulation model as shown in Fig. 6(a). Close agreement of the variation of the heating current with the applied voltage for both the measured resonator prototype and its FE simulated model is shown in Fig. 6(b). The measured resonator quality with heating power is shown in Fig. 7(a) while the simulated resonator temperature change with heating power is presented in Fig. 7(b).

DOI: https://doi.org/10.26799/cp-sms-nanomed-sensors-egf-2024

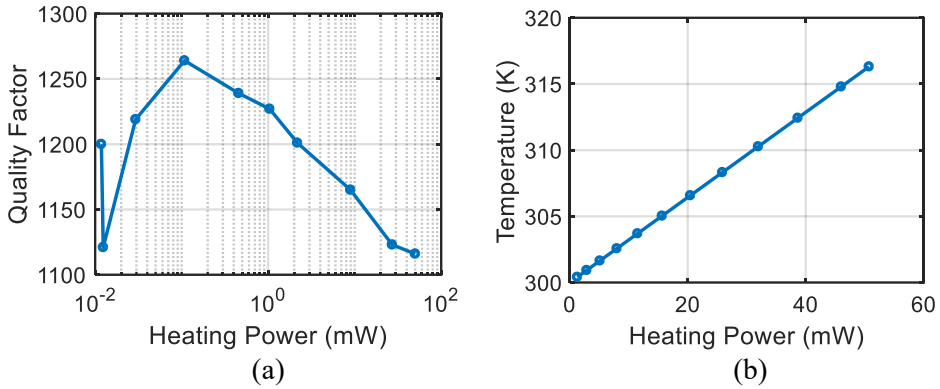

Fig. 7: (a) Variation of the measured resonator quality factor with heating power (b) Variation of the simulated resonator temperature with heating power.

4. Conclusion

This paper presented the experimental investigation of electrothermal fine frequency tuning for a 60 MHz laterally excited contour mode bulk acoustic wave MEMS resonator. Frequency tuning is achieved via electrothermal SOI bulk heating of the resonator. Experimental results show that the resonant frequency decreases with an increase in the electrical heating power, which is applied to the resonator SOI bulk via two heating electrodes. For a 50-mW heating power swing, the resonator frequency varies from 61.368 MHz to 61.418 MHz. The measured results are supported and corroborated via finite element modelling and simulation.

Acknowledgements

The authors would like to acknowledge the Ministry of High Education in Libya for supporting the doctoral research work of Munira Bengashier, which is currently being carried out at the University of Malta.

References

1. B. Sviličića, "Tunability of Piezoelectric MEMS Ring Resonator Based Filter", *Procedia Engineering*, vol. 168, pp. 1517-1520, 2016.
2. X. Lia, Y. Huanga, Y. Dub, Z. Lib, F. Baoa and J. Baoa, "Study of a 10 MHz MEMS oscillator with a TPoS resonator", *Sensors and Actuators A*, vol. 258, pp. 59-67, 2017.
3. A. Tazzoli, M. Rinaldi and G. Piazza, "Ovenized High Frequency Oscillators based on Aluminium Nitride Contour-mode MEMS resonators", *In Proceedings of the 2011 IEEE International Electron Devices Meeting*, Washington DC, USA, 2012, pp. 1-4.
4. W. Zhang, K. Hu, Z. Peng and G. Meng, "Tunable Micro-and Nanomechanical Resonators", *Sensors*, vol. 15(10), pp. 26478-26566, 2015.
5. M. Bengashier, I. Grech, O. Casha, B. Portelli and R. Farrugia, "Experimental Validation of Tuning Mechanisms Applied on AlN Piezoelectric Contour Mode MEMS Resonators", *In Proceedings of the 2020 IEEE Symposium on Design, Test, Integration and Packaging of MEMS/MOEMS (DTIP 2020)*, Lyon, France, 2020, pp. 1-4.
6. A. Cowen, G. Hames, K. Glukh, and B. Hardy, "PiezoMUMPs Design Handbook", Durham, NC, USA: MEMSCAP Inc, 2014.
7. M. Bengashier, I. Grech, O. Casha, B. Portelli, R. Farrugia and E. Gatt, "A Feasibility Study on Piezoelectric MEMS Lateral Bulk Acoustic Wave Resonators including Thermal Effect", *In Proceedings of the 2019 Symposium on Design, Test, Integration and Packaging of MEMS and MOEMS (DTIP 2019)*, Paris, France, 2019, pp. 1-5.
8. U. Gysin, S. Rast, P. Ruff, E. Meyer, D. W. Lee, P. Vettiger, C. Gerber, "Temperature Dependence of the Force Sensitivity of Silicon Cantilevers", *Physical Review B*, vol. 69(4), pp. 45403, 2004.

Proceedings of the Sensors 2024 International Conference
Barcelona, Spain, 23 – 25 October 2024
DOI: https://doi.org/10.26799/cp-sms-nanomed-sensors-egf-2024

Impact of Optical Fiber Design on the Performance of Interferometric Temperature Sensors at Elevated Temperatures

S. Pevec [1*], M. Njegovec [1], V. Budinski [1], V. Žužek[2], J. Bojkovski[2], D. Donlagic [1]

[1]Faculty of Electrical Engineering and Computer Science, University of Maribor, Slovenia
[2] Faculty of Electrical Engineering, University of Ljubljana, 1000 Ljubljana, Slovenia

Abstract

In this article we investigate the impact of the optical fiber core design and composition on the performance of fiber-based interferometric temperature sensors at elevated temperatures. A collection of commercially available single-mode fibers with different core designs and compositions were configured into otherwise nearly identical Fabry-Perot temperature sensors, which were then systemically tested for drift at a range of elevated temperatures between 200 and 800 °C. Results indecent that sensor drifts correlate to core doping levels and fiber designs. In some fibers, significant drifts were observed even at temperatures below 400 °C, while all sensors exhibited significant drifts at temperatures above 600 °C. Aggressive annealing demonstrated substantial sensors stability improvement but did not fully eliminate drifts.

Keywords: Optical fibers, temperature sensor, high-temperature, Fabry-Perot, fiber design, capillary based packaging.

1. Introduction

Temperature measurements play a critical role in ensuring product quality, optimizing processes, and safeguarding human health. The continual evolution of temperature measurement technologies con-tributes to improved accuracy, efficiency, and adaptability, making them indispensable tools in vari-ous sensors systems.

In challenging environmental conditions, intrinsic optical fiber temperature sensors like fiber Bragg gratings [1], and Fabry-Perot interferometers (FPI) [2] have been demonstrated as suitable and to some extend robust measuring principles. Limitations arise mainly at elevated temperatures above 600 °C. To date, many different principles have been demonstrated to build a fiber-optic sensor that can operate reliably at temperatures above 700 °C. Still, many solutions involve either sapphire fibers [3] or specialty fibers [4] that are not commercially available or are very expensive. Most authors agree that drifts are mainly related to the optical fiber properties, which are defined at the optical fiber manufacturing stage [5]. In the manufacturing process, a waveguide is formed in the fiber, which in the case of standard single-mode fiber consists of a Ge-doped core surrounded by pure SiO_2 cladding. Difference between the core and the cladding allows two mechanisms to lead to changes in the effective refractive index of the core as the temperature rises. The first mechanism is related to the residual stresses between the core and the cladding, which are due to the different temperature expansions between the core and the cladding. Namely, when the fiber cools down, in the case of a standard single-mode fiber, the core will have residual mechanical stresses between core and clad-ding. The core will undergo decompression, which decreases the refractive index of the core (when the fiber is heated up considerably, there is a relaxation of the tension, and the refractive index will slowly increase as a result). The second mechanism is related to the diffusion of dopants. Elevated temperatures will cause the dopant to diffuse in or out of the fiber core, which changes the refractive index distribution of the fiber waveguide, thereby changing the optical properties of the temperature sensor [6].

In this work we analyze the stability of Fabry-Perot optical fiber sensors, constructed from four different types of commercially available optical fibers, differing in dopant concentration and composition (three Ge doped fibers and one F doped fiber).

2. Sensor design

The sensor shown in Fig. 1 utilize Fabry-Perot Interferometer (FPI) constructed between two semi-reflective H_fO_2 mirrors, placed on the tip of a large 200 □m lead-in single mode optical fiber (SMF). Large 200 □m diameter lead-in fiber was extended with short section of standard 125 □m SMF, which

Proceedings of the Sensors 2024 International Conference
Barcelona, Spain, 23 – 25 October 2024
DOI: https://doi.org/10.26799/cp-sms-nanomed-sensors-egf-2024

ensures an airgap between the capillary wall and the sensor wall (Fig. 1c), thereby ensuring no strain transfer to the sensor cavity.

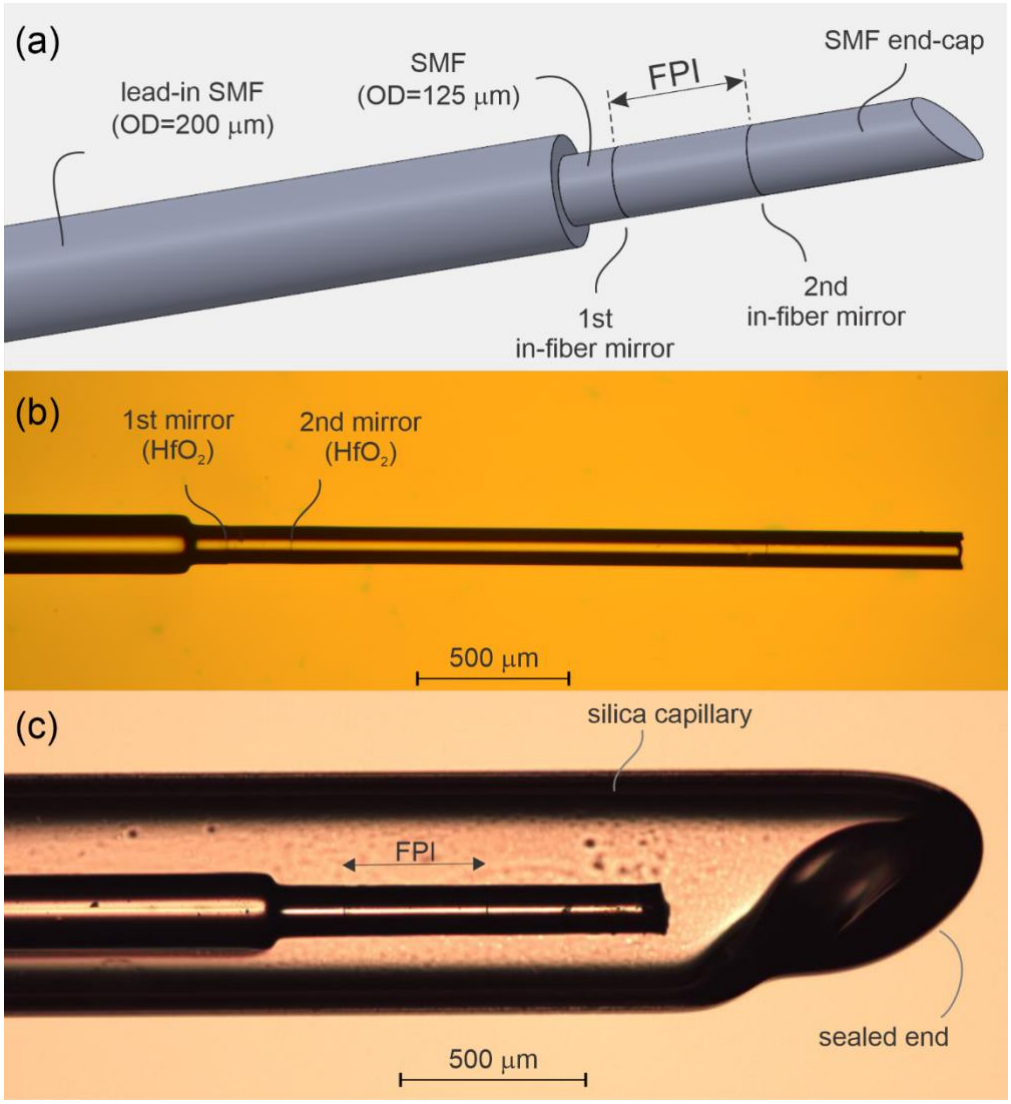

Fig. 1: Temperature sensor: (a) sensor design, (b) optical image of typical fabricated sensor, (c) sensor packaged in quartz capillary.

3. Results

Four different groups of commercially available single mode fibers (Tab.1) were systemically tested for drift at a range of elevated temperatures between 200 °C and 800 °C.

Table.1: Sensor's fibers:

Sensor's fiber type	NA	MFD at 1550 nm	Dopant type
SMF (YOFC)	0.14	10.3	Ge (Core)
UHNA3 (Thorlabs)	0.35	4.1	Ge (Core)
LMA20/125 (Coherent)	0.08	21.9	Ge (Core)
S1310 (Coherent)	0.12	10.4	F (Cladding)

All sensors (8 sensors; two sensors for each group) were tested in the SIKA TP2885E temperature calibrator (Fig. 2b), which allows temperature control up to 850°C. First, sensors were tested immediately after production to verify what can be obtained without additional stabilization/annealing

DOI: https://doi.org/10.26799/cp-sms-nanomed-sensors-egf-2024

treatments. The entire test cycle was carried out at temperatures ranging from 200 °C to 800 °C with a step increments of 100 °C (Fig. 2a).

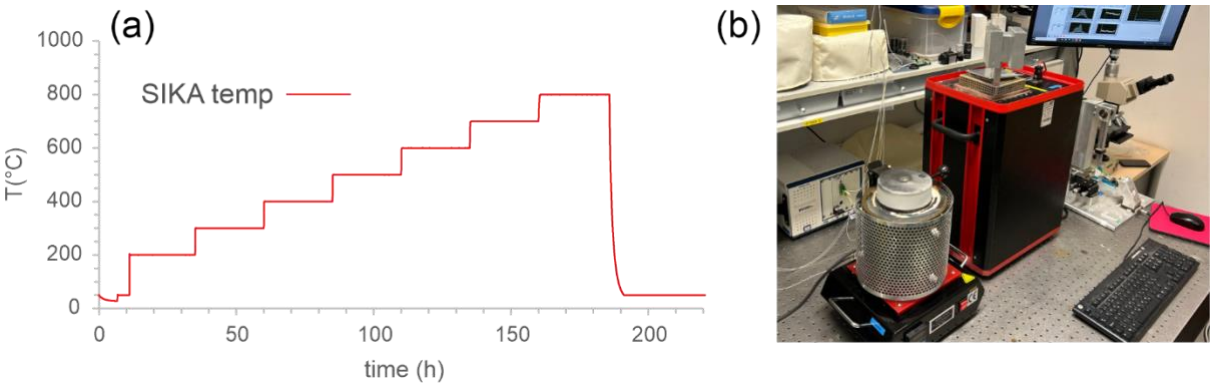

Fig. 2: Testing procedure and key equipment: (a) temperature time curve for typical test cycle, (b) SIKA TP2885E temperature calibrator and MF-2000 melting furnace.

Temperature drifts were monitored for 24 hours at each temperature set point as presented in Fig. ***3***.

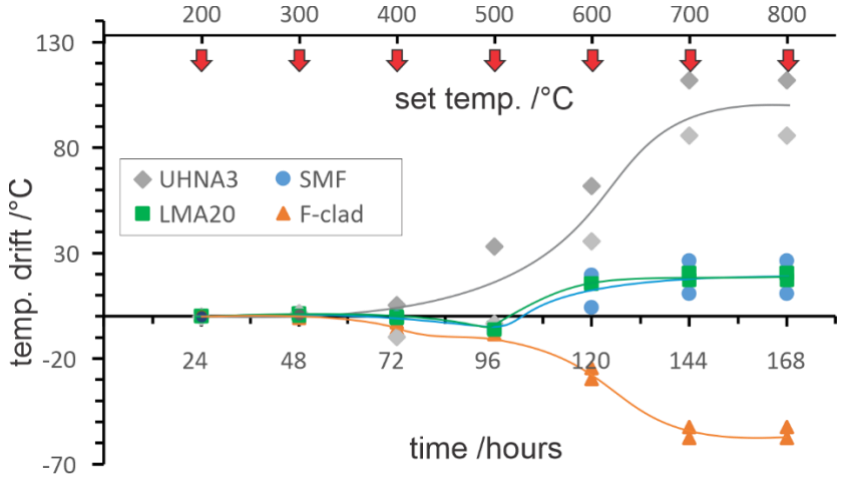

Fig. 3: Graph of temperature drift vs time and set temperature for different types of sensors tested immediately after sensor production.

Results indicate that sensor drifts correlate to core doping levels and fiber designs. In highly doped Ge fiber and F doped fiber, significant cumulative drifts of 2°C were observed even at temperatures below 400 °C, while all sensors exhibited significant drifts at temperatures above 500 °C. In the case of the most Ge-doped fiber UHNA3 and F-doped fiber S1310, commutative drift was exceeded 100 °C and -60 °C respectively. The further investigation utilized annealing of sensors at a maximum temperature that did not cause significant fiber devitrification (at 1000 °C). After annealing at 1000 °C for 24 hours sensors were tested again under the same conditions as in the first cycle. The final results are presented in Fig. 4

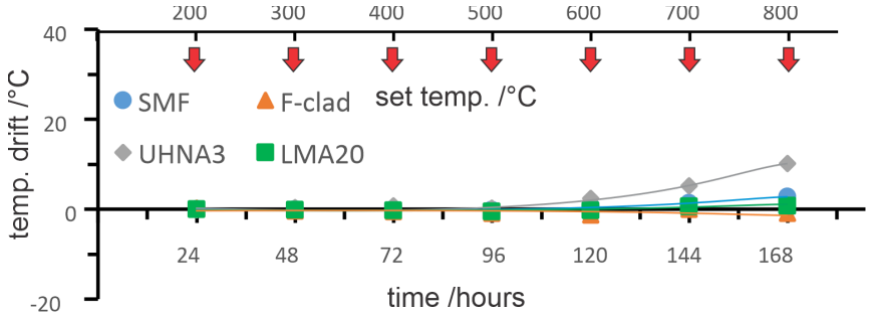

Fig. 4: Graph of temperature drift vs time and set temperature for different types of sensors tested after 24 hours annealing treatment @ 1000°C.

DOI: https://doi.org/10.26799/cp-sms-nanomed-sensors-egf-2024

After 24 hours of annealing, the results showed significant improvement. Although the sensors with the high-Ge core fiber (UHNA 3) exhibited a slight drift of 10 °C over the entire heating cycle up to 800 °C, the other sensors maintained an overall drift below 3 °C.

4. Conclusion

All annealed sensors demonstrated substantial improvement in their stability at elevated temperatures, even if they were submitted to relatively fast cooling cycles. However, even with this aggressive annealing procedure, while it reduces drifts and thus potentially extended applicable operating temperature ranges, it did not completely eliminate issues with the drifts at the high end of the attainable operating temperature range. A clear correlation of the sensor drifts to fiber core compositions, however, points towards potential opportunities where specialty optical fibers with modified core composition might further improve the performance of interferometric sensors (and FBGs) performances at the highest operating temperatures.

Acknowledgements

This research was funded by EURAMET, INFOTherm (Grant No. 22IEM07) and Slovenian Research Agency (ARIS) under grant no. P2-0368.

References

1. D. Grobnic, C. Hnatovsky, S. Dedyulin, R. B. Walker, H. M. Ding, and S. J. Mihailov, "Fiber Bragg Grating Wavelength Drift in Long-Term High Temperature Annealing," Sensors-Basel 21, 1-28 (2021). doi: 10.3390/s21041454
2. Z. S. Chen, et al., "High-Temperature Sensor Based on Fabry-Perot Interferometer in Microfiber Tip," Sensors-Basel 18(2018). doi:10.3390/s18010202
3. P. F. Chen, F. F. Pang, Z. W. Zhao, L. Hong, N. Chen, Z. Y. Chen, and T. Y. Wang, "Fabry-Perot cavity based on sapphire-derived fiber for high temperature sensor," 24th International Conference on Optical Fibre Sensors 9634(2015). doi:10.1117/12.2194528
4. S. C. Warren-Smith, L. V. Nguyen, C. Lang, H. Ebendorff-Heidepriem, and T. M. Monro, "Temperature sensing up to 1300°C using suspended-core microstructured optical fibers," Opt Express 24, 3714-3719 (2016). doi:10.1364/Oe.24.003714
5. U. C. Paek and C. R. Kurkjian, "Calculation of Cooling Rate and Induced Stresses in Drawing of Optical Fibers," J Am Ceram Soc 58, 330-335 (1975). doi: 10.1111/j.1151-2916.1975.tb11490.x
6. D. Polyzos, J. Mathew, W. N. MacPherson, and R. R. J. Maier, "Effect of Dopant Diffusion on the Long-Term Stability of Fabry-Perot Optical Fiber Sensors," J Lightwave Technol 35, 5317-5323 (2017). doi:10.1109/Jlt.2017.2773501